Applied Materials Today 48 (2026) 103018

Contents lists available at ScienceDirect

Applied Materials Today

journal homepage: www.elsevier.com/locate/apmt

3D-printable ionic liquid formulations for filler-free, transparent ion-conducting soft materials

Rosario Carmenini [a], Alberto Sanz de Leon [b], Mauro Comes Franchini [a], Sergio Ignacio Molina [b], Mirko Maturi [b,*]

[a] Department of Industrial Chemistry "Toso Montanari", University of Bologna, Bologna 40136, Italy
[b] Dpto. Ciencia de los Materiales, I. M. y Q. I., IMEYMAT, Facultad de Ciencias, Universidad de Cádiz, Campus Río San Pedro, s/n, 11510 Puerto Real, Cádiz, Spain

ARTICLE INFO

Keywords:
Vat photopolymerization
Photocurable ionic liquids
Ion-conducting polymers
Transparent soft materials
Process–structure–property relationships

ABSTRACT

This work presents a family of photocurable ionic liquids (pILs) based on a polymerizable methacrylate anion and readily available organic cations, designed for vat photopolymerization (VP) of soft ion-conducting networks. The pILs were synthesized by straightforward ion exchange, providing liquid salts that are fully compatible with commercial acrylate resins and enable filler-free 3D printing of transparent ionic polymers. By systematically mapping the resin compositions as a function of the total acrylate content and the fraction of crosslinking species, a clear printability window was identified, allowing prediction of the maximum printable ionic liquid concentration from the molecular weight of the chosen cation. Mechanical properties were shown to be governed primarily by network architecture, with imidazolium-based systems displaying linear correlations between stiffness and crosslinking density, while tetraalkylammonium cations introduced exponential softening due to their plasticizing effect. In contrast, ionic conductivity was largely dictated by cation size, hydrophobicity, and charge shielding, enabling conductivity values in the 10^{-6}–10^{-4} S/cm range without the need for conductive fillers. These results demonstrate a chemically simple and generalizable approach to obtain printable, filler-free ion-conducting materials, opening opportunities for applications in antistatic coatings, electrostatic discharge protection, flexible and stretchable sensors, and low-voltage energy harvesting devices.

1. Introduction

The field of polymer additive manufacturing (AM), the bottom-up construction of three-dimensional structures through spatially controlled physical or chemical processing of base polymers, is rapidly expanding toward new materials and composites that enhance mechanical performance and add targeted functionalities for specialized sectors including automotive, aerospace, biomedicine, and electronics [1–3]. Among AM technologies, vat photopolymerization (VP) is especially versatile: it converts liquid monomer mixtures into solid 3D objects with high resolution and dimensional accuracy via spatially confined photopolymerization [4–6]. In VP, the properties of printed parts are largely dictated by resin chemistry, and functionalities such as luminescence, piezoelectricity, and electrical conductivity can be introduced by adding photoreactive or inert molecular or nanostructured species to photocurable resins, enabling their physical or chemical entrapment in the crosslinked matrix during curing [7,8].

Ionogels are hybrid materials in which an ionic liquid (IL) is confined within a solid or polymeric matrix, combining the advantages of ILs with the mechanical stability of polymer networks [9]. They retain essential IL features such as high ionic conductivity, wide electrochemical stability window, negligible vapor pressure, and thermal stability, while exhibiting the processability and robustness of solid-state materials [10]. Owing to this combination, ionogels have been widely explored as solid electrolytes for lithium batteries and supercapacitors and as functional components in electrochromic devices, soft actuators, flexible sensors, and wearable electronics [11–15]. Their versatility stems from the independent tunability of the IL composition and the host matrix, enabling tailored materials for energy storage, optoelectronics, and emerging flexible technologies. For these reasons, ionogels have attracted growing attention in AM (specifically VP), where coupling ionic conductivity with structural stability opens opportunities for fabricating functional devices with complex geometries [16,17].

Incorporating ILs into photocurable matrices allows ionogels to be

* Corresponding author at. Dpto. Ciencia de los Materiales, I. M. y Q. I., IMEYMAT, Facultad de Ciencias, Universidad de Cádiz, 11510 Puerto Real, Cádiz, Spain.
E-mail address: mirko.maturi@uca.es (M. Maturi).

https://doi.org/10.1016/j.apmt.2025.103018
Received 18 October 2025; Received in revised form 4 November 2025; Accepted 27 November 2025
Available online 2 December 2025

processed by VP into tailored solid-state electrolytes, stimuli-responsive components, or flexible electronic elements [18]. This strategy leverages tunability in both the IL (e.g., viscosity, ionic conductivity, electrochemical stability) and the photocurable network (e.g., mechanical robustness, flexibility, permeability), providing a versatile route to advanced materials for energy storage devices, electrochemical sensors, and soft robotics [19]. A major limitation of ionogels obtained by simply adding free ILs, however, is leakage of the liquid phase, because ionic species are not covalently anchored to the polymer network. This can reduce long-term stability, cause performance loss, and contaminate neighboring components in practical devices [20]. In addition, the plasticizing effect of ILs often compromises mechanical integrity, making printed structures more fragile or prone to deformation [21,22]. Phase separation between polymer and IL during curing or operation may also occur, negatively affecting both printability and ionic conductivity, especially if a percolation threshold is not efficiently achieved [23,24]. For example, VP resins containing up to 50 wt % 1-butyl-3-methylimidazolium bis(trifluoromethanesulfonyl)imide (BMIMTFSI) yielded 3D-printed materials with ionic conductivity in the 10^{-6}–10^{-4} S/cm range and improved strength, but required very high IL fractions [25]. Because the IL is not chemically bound to the network, potential leaching, dimensional instability, and reduced durability may arise. Moreover, an intrinsic trade-off between conductivity and mechanical integrity persists, and the need for such high IL content narrows formulation space and limits tunability. The chemical design is also relatively complex: the non-ionic polymer backbone requires non-trivial synthetic steps, while the IL relies on a fluorinated imide anion that is synthetically demanding and not particularly sustainable.

These drawbacks have been partially addressed by developing ionic liquids whose cations co-polymerize during VP, becoming covalently integrated into the polymer network [26,27]. This approach minimizes IL leakage, improves long-term stability, and enhances compatibility between ionic domains and the photocurable matrix, but tends to reduce achievable room-temperature conductivities due to single-ion transport. Alternative approaches to minimize IL leakage include physical confinement within crosslinked polymer networks or inorganic matrices, the use of polymer–IL blends forming bicontinuous morphologies, and the grafting of polymer brushes to retain ionic liquids by capillary forces [28–30]. While these methods partially mitigate leakage, they often result in complex formulations or microphase separation, limiting optical clarity and printability. In contrast, covalently integrating ionic moieties through polymerizable ILs ensures structural stability and compositional homogeneity without sacrificing processability. Polymerized-IL membranes have been investigated as anion-exchange electrolytes in alkaline fuel cells, enabling efficient anion transport and serving as key cell components [31,32]. Beyond membranes, polymerized ILs have been explored as binders in solid-state supercapacitors, improving electrode–electrolyte interfaces and ion transport; for example, incorporating polymerizable ILs into graphene-based electrodes enhances contact with the liquid electrolyte, facilitating ion diffusion and increasing specific capacitance by up to ~130 % [33,34]. Although polymerizable ionic liquids have been previously investigated, typically involving polymerizable cations such as vinylimidazolium or acrylate-functionalized ammonium salts, no studies have, to our knowledge, reported the use of polymerizable anions (e.g., methacrylate-based) in formulations designed for additive manufacturing. The present approach therefore introduces a complementary and chemically design, in which readily simpler available cations are paired with a methacrylate anion, enabling direct incorporation of the ionic species into photocurable resins for vat photopolymerization without complex synthesis or additional additives.

In this work, we report the development of a family of simple, photocurable ionic liquids (pILs) composed of a polymerizable methacrylate anion and readily available organic cations, and their formulation with commercial VP components to obtain soft, 3D-printed ionic polymers with tunable ionic conductivity and mechanical properties. The ionic liquids were prepared by straightforward ion exchange from halogenated precursors and are compatible with standard acrylate resins, enabling filler-free printing under conventional VP conditions. The resulting materials combine MPa-level stiffness with elongations typical of soft networks and deliver room-temperature ionic conductivities in ranges relevant to antistatic and sensing applications, while preserving the simplicity and scalability of their chemistry. To rationalize performance and guide formulation, materials printability and properties are analyzed as functions of resin composition and crosslinked network architecture using two physically meaningful descriptors: the total acrylate content per gram and the fraction contributed by multifunctional crosslinkers. Mapping compositions in this space reveals a printability window and composition trajectories governed by the molecular weight of the ionic liquid, providing predictive levers for maximizing printable ionic content without sacrificing network integrity. Within this framework, mechanical response is predominantly controlled by network architecture, whereas ionic transport is governed by cation structure, enabling independent optimization of stiffness and conductivity. The approach is general and expandable through cation choice, ionic or macro-crosslinkers, and low-molecular-weight reactive diluents, and is positioned to deliver high-performance, filler-free ion-conducting materials for diverse use cases, including stretchable and pressure sensors, antistatic and electrostatic-discharge control, supercapacitor components, and low-voltage energy-harvesting interfaces.

2. Materials and methods

If not otherwise specified, reagents and solvents were purchased from Sigma Aldrich (St. Louis, MO, USA) and used as received. Poly (ethylene glycol) methyl ether acrylate (PEGMA, $n = 9$), poly(ethylene glycol) diacrylate (PEGDA, $n = 9$), 1-ethyl-3-methylimidazolium chloride ([C_2MIM]Cl), and tetraethylammonium chloride ([N_{2222}]Cl) were purchased from TCI Europe (Zwijndrecht, Belgium). 1-hexyl-3-methylimidazolium chloride ([C_6MIM]Cl), 1-decyl-3-methylimidazolium chloride ([C_{10}MIM]Cl), and tetraoctylammonium bromide ([N_{8888}]Br) were purchased from Fluorochem Ltd (Glossop, UK).

2.1. Silver-mediated synthesis of photocurable ionic liquids (pILs)

In a typical procedure, methacrylic acid (1 mol, 86.1 g) was placed in a 500 mL round-bottomed flask under magnetic stirring and in a N_2 atmosphere and diluted with 150 mL of a solvent 1. Then, solid Ag_2O (0.55 mol, 127 g) was added, and the mixture was stirred at 70 °C for one hour to allow for the formation of silver methacrylate. The mixture was filtered over celite, placed in another flask and titrated with a solution of the selected halide ionic liquid (1 mol in 250 mL of solvent 2), until no silver halide was observed forming upon addition of IL. Then, the mixture was filtered over celite to remove the silver salts. From the clear solution, the organic solvents were removed by rotary evaporation, while water was removed by freeze-drying.

In the case of highly lipophilic cation ($[N_{8888}]^+$), the purification was performed by solvent extraction after the removal of the organic solvents by rotary evaporation. In fact, the aqueous phase was extracted three times with ethyl acetate (3 × 100 mL) and dried to achieve the isolated pILs.

Details of the reaction yields and solvents used for each of the synthetized pILs are provided in Table S1.

2.2. Silver upcycling

To convert the silver waste back to Ag_2O, the separated silver halide was washed with 1 L of a 2 M HNO_3 solution to remove photoreduced Ag, filtered and dispersed in 200 mL of water, which was alkalinized using solid NaOH and NH_4OH. At this point, hydrogen peroxide (30 vol. %) was added dropwise to produce solid Ag^0, until no more O_2 was formed. The mixture was then filtered, and the solid was dispersed in the

HNO_3 solution used previously. To the same solution, the Ag_2O-loaded celite from the synthesis of silver methacrylate was added, and the mixture was boiled for 1 h to ensure the solubilization of all silver species as $AgNO_3$. Once clear, the mixture was cooled, filtered to remove cleaned celite, and treated with an excess of NaOH to neutralize the acid and to convert silver nitrate into Ag_2O, which was removed by filtration, dried and upcycled. Recovery yield = 94 %

2.3. Ag-free synthesis of photocurable ionic liquids (pILs)

In a typical procedure, potassium methacrylate (1 mol, 124.2 g) and the selected halide ionic liquid (1 mol) were placed in a 1-L round-bottomed flask followed by the addition of 500 mL of the proper mixture of solvents and stirred overnight at room temperature. For pILs produced using MeCN/Toluene as the solvents, MeCN was removed under reduced pressure to reduce the solubility of potassium halide, which was then separated by filtration. For pILs prepared using MeCN/EtOH, an excess of acetone was added to reduce the solubility of the potassium halide, which was then filtered out. The ILs were finally recovered by removing the organic solvent under reduced pressure. In the case of highly lipophilic cation ($[N_{8888}]^+$), the purification was performed by solvent extraction after the addition of an excess of water at the end of the reaction time. In fact, the aqueous phase was extracted three times with ethyl acetate (3 × 100 mL) and dried to achieve the isolated pILs.

Details of the reaction yields and solvents used for each of the synthetized pILs are provided in Table S2.

2.4. Computed cation properties

The molecular structures of the investigated cations were built and subjected to geometric optimization using the MM2 force field to obtain their equilibrium three-dimensional conformations. The molecular volume was then estimated as Connolly Volume, i.e., the volume enclosed by the solvent-accessible molecular surface. Calculations were performed ChemOffice Professional (v23.1.1.3, Revvity, USA), using the default probe radius of 1.4 Å, corresponding to the van der Waals radius of a water molecule.

The lipophilicity of the investigated cations was estimated as octanol-water partition coefficients (cLogP) using the same software. Calculations were carried out with the BioByte fragment-based algorithm, which assigns empirically derived fragment constants to estimate the hydrophobic contribution of each structural unit. Given that imidazolium and quaternary ammonium salts are permanently charged species, the reported cLogP values do not correspond to experimental partition coefficients in octanol/water systems but rather serve as computational descriptors of relative hydrophobicity.

2.5. Resins formulation and VP

A blank photocurable resin (1 kg) was prepared by mixing 300 g of isobornyl acrylate (IBOA), 50 g of 1,6-hexanediol diacrylate (HDDA), 200 g of poly(ethylene glycol) diacrylate (PEGDA, $n = 9$), 300 g of poly (ethylene glycol) methyl ether acrylate (PEGMA, $n = 9$), and 150 g of 2-hydroxyethyl methacrylate (HEMA). This base formulation was subsequently combined with different pILs at varying proportions, as reported in Table 1, to obtain final ionic liquid concentrations of 0.5, 1.0, 1.5, 2.0, 3.0, 3.5, and 4.0 mmol/g. The highest achievable molar concentration was limited by the molecular weight of each pIL. This approach allowed to keep constant the proportions between the weight contents of IBOA, HDDA, PEGDA, PEGMA and HEMA, and equal to 6:1:4:6:3, respectively. To 100 g of each resin, 2 g of phenylbis(2,4,6-trimethylbenzoyl) phosphine oxide (BAPO) were added as the photopolymerization initiator and 1 g of 4-methoxyphenol were added as the radical stabilizer. After thorough magnetic stirring of the mixture to ensure the complete dissolution of the solid additives, the mixture was briefly degassed by sonication (2 min) and poured in the vat of a Phrozen Mini 8 K S desktop VP 3D printer working with a 405 nm LCD-LED screen with a XY resolution of 22 μm. Irradiation time was 30 s for the base layers and 20 s for the consecutive ones. Computer-assisted design (CAD) files of tensile testing specimens according to ISO 37 (type 2), and electrical conductivity specimens according to ASTM D257 were sliced using Chitubox v1.9.5 software. The 3D-models were converted into a GCODE file suitable for 3D printing. The printed objects were then separated from the printer platform and washed with isopropyl alcohol to remove unreacted resin. Postprocessing of the samples was carried out for 60 min at 60 °C in a chamber equipped with a 405 nm light source and a power of 1.25 mW/cm2 (FormCure, Formlabs).

Table 1
Detailed composition of the prepared pIL-based VP formulations. C = molar concentration of pIL.

Cation	C (mmol/g)	pIL (wt. %)	IBOA (wt. %)	HDDA (wt. %)	PEGDA (wt. %)	PEGMA (wt. %)	HEMA (wt. %)
-	-	-	30.0	5.0	20.0	30.0	15.0
$[C_2MIM]^+$	0.5	9.8	27.0	4.5	18.0	27.0	13.5
	1.0	19.6	24.1	4.0	16.0	24.1	12.0
	1.5	29.4	21.2	3.5	14.1	21.2	10.6
	2.0	39.3	18.2	3.0	12.2	18.2	9.1
	3.0	58.9	12.3	2.0	8.2	12.3	6.2
	3.5	68.7	9.4	1.6	6.3	9.4	4.7
	4.0	78,5	6,45	1075	4,3	6,45	3225
$[C_6MIM]^+$	0.5	12.6	26.2	4.4	17.5	26.2	13.1
	1.0	25.2	22.4	3.7	15.0	22.4	11.2
	1.5	37.9	18.6	3.1	12.4	18.6	9.3
	2.0	50.5	14.9	2.5	9.9	14.9	7.4
	3.0	75.7	7.3	1.2	4.9	7.3	3.6
$[C_{10}MIM]^+$	0.5	15.4	25.4	4.2	16.9	25.4	12.7
	1.0	30.8	20.7	3.5	13.8	20.7	10.4
	1.5	46.3	16.1	2.7	10.7	16.1	8.1
	2.0	61.7	11.5	1.9	7.7	11.5	5.7
	3.0	93	2,3	0,4	1,5	2,3	1,1
$[N_{2222}]^+$	0.5	10.8	26.8	4.5	17.8	26.8	13.4
	1.0	21.5	23.5	3.9	15.7	23.5	11.8
	1.5	32.3	20.3	3.4	13.5	20.3	10.2
	2.0	43.1	17.1	2.8	11.4	17.1	8.5
	3.0	64.6	10.6	1.8	7.1	10.6	5.3
	3,5	75,4	7,38	1,23	4,92	7,38	3,69
$[N_{8888}]^+$	0.5	27.6	21.7	3.6	14.5	21.7	10.9
	1.0	55,2	13,5	2,2	9.0	13,4	6,7

2.6. Materials characterization

^{1}H NMR spectra were recorded on a Bruker 500 MHz spectrometer using DMSO-d6 as the solvent for all samples. In all recorded spectra, chemical shifts are reported in parts per million of frequency relative to the residual solvent signals (2.50 ppm, quintet, $J_{HD} = 1.9$ Hz). ATR-FTIR analyses were performed with a PerkinElmer Spectrum Two spectrophotometer, equipped with a Universal ATR accessory; all spectra were recorded as an average of 20 scans (range 4000−400 cm^{-1} with a resolution of 0.5 cm^{-1}). The transparency of the 3D-printed materials to visible light was evaluated in the 400–800 nm range using a Cary 50 single-beam spectrophotometer (Agilent), with a 1-mm-thick specimen placed in the beam pathway. Water content of 3D printed materials was determined by precisely weighing around 5 g of material 1 week and 6 months after their manufacturing, before and after a thermal treatment at 100 °C in a vacuum over until constant weight was achieved. Total water content ($w_{\%}$) was calculated as the ratio between the mass loss and initial sample mass. Gravimetric analysis was performed on three replicates for each analysed ionomer. Degree of curing ($DC_{\%}$) was assessed via determination of gel content accounting for the previously determined water content. Typically, a precise amount of 3D printed material (around 2 g) soaked in MeOH for 24 h at room temperature, then filtered and dried at 60 °C in a vacuum oven until constant weight. The degree of curing was then calculated according to Eq. (1):

$$DC_{\%} = \frac{m - m_0}{m_0} + w_{\%} \quad (1)$$

Where m_0 is the initial mass of the sample and m is its mass after treatment with MeOH and drying. The test was repeated on three independent samples for each 3D printed composition, and data are reported as mean ± SD. The mechanical properties of the printed materials were measured in a Shimadzu AGS-X universal testing machine. Tensile testing of the specimens was carried out at 2 mm/min, and, for each printed composition, five independent samples were tested, and the results were reported as mean ± SD.

Electrical conductivity (κ) was determined at room temperature using a Keithley 6517B electrometer (Keithley, Cleveland, OH, USA) equipped with a parallel-plate test fixture with graphite electrodes. Disc-shaped samples were placed between the electrodes, and the instrument directly provided the volume resistivity (ρ) value, which was then converted into volume conductivity (κ) as $\kappa = 1/\rho$. Since the samples exhibited a wide range of conductivities, the applied voltage was adjusted depending on the material in order to maintain the measured current within the operating range of the electrometer (avoiding both noise-limited and overrange conditions). For each material, the ohmic behavior was verified by recording current values at four different voltages and confirming linearity; the conductivity values were then taken from the standard resistivity measurement mode of the instrument. A stabilization time of 60 s was allowed before each measurement, following ASTM D257. For each printed composition, three independent samples were measured, and the data were expressed as mean ± SD.

3. Results and discussion

Large-scale synthesis of methacrylated photocurable ionic liquids (pILs) was achieved via ion exchange reactions between aprotic organic halide salts and silver methacrylate (Fig. 1a). This process led to the precipitation of silver halide (AgX) and the concurrent formation of the desired organic methacrylate salt in solution, which was subsequently purified and isolated. A range of cationic structures was investigated to

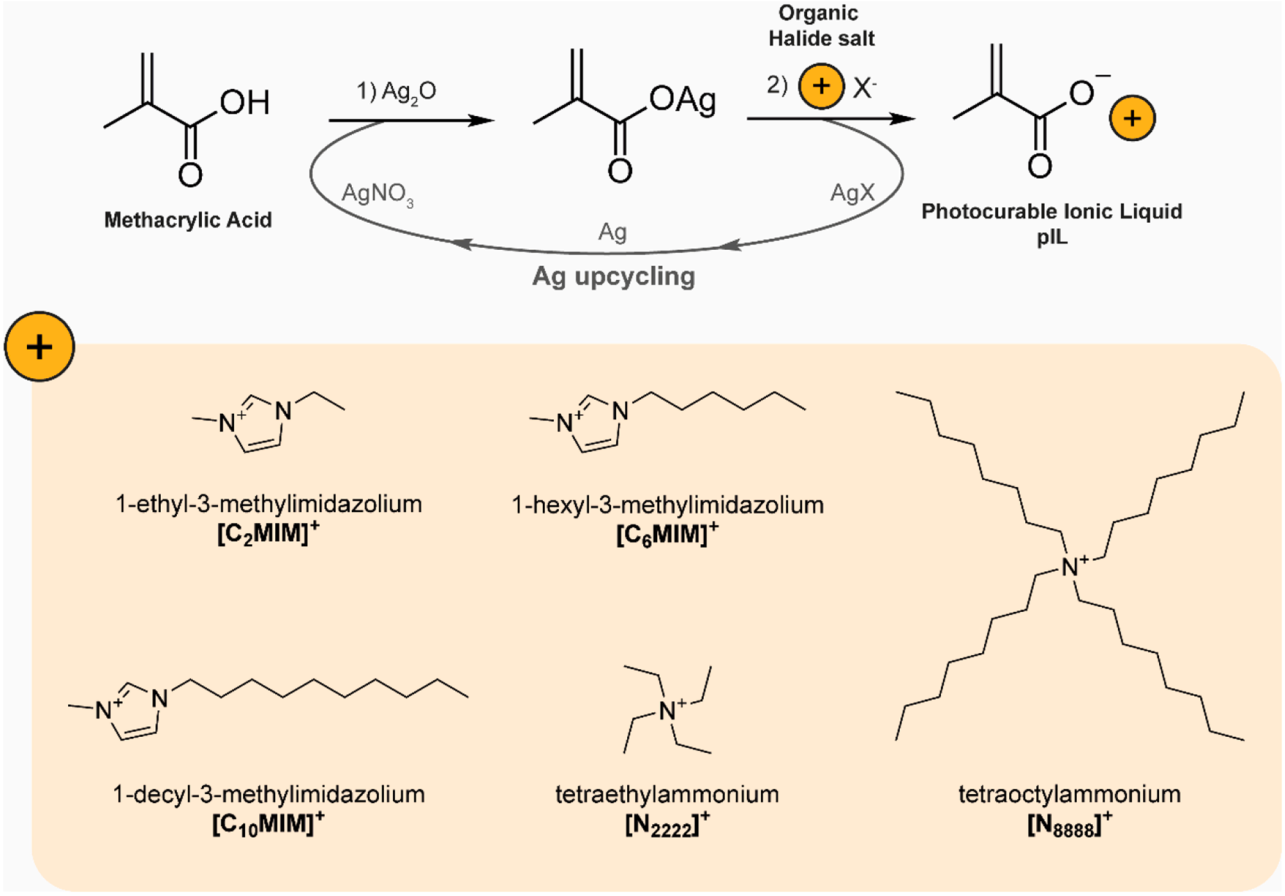

Fig. 1. Synthesis of photocurable ionic liquids (pILs). General representation of the employed ion exchange reaction (top) and chemical structure of the selected cations (bottom).

explore the influence of molecular features such as ionic size, geometry, and lipophilicity (Fig. 1b). The main drawbacks of this synthetic route (poor atom economy and the generation of stoichiometric quantities of silver halide waste), were addressed through two complementary strategies. First, a reproducible upcycling procedure was developed to recover silver oxide from AgX. This involved treating the silver halide with aqueous ammonia and hydrogen peroxide under alkaline conditions to reduce AgX to elemental silver (Ag^0), followed by oxidative dissolution in nitric acid and precipitation of Ag_2O using NaOH (Figure S1). This recycling pathway enabled the recovery of up to 94 % of the silver used, producing environmentally benign byproducts such as NaX and $NaNO_3$, while NO_2 emissions could be mitigated through appropriate trapping systems.

In parallel, an alternative synthetic approach was developed by substituting silver methacrylate with potassium methacrylate, as a proof-of-concept for a future, more sustainable synthetic pathway. This method, even though it proved to be less efficient for cations of higher polarity (Table S2), enabled the preparation of ILs on a large scale (up to 2 mol) and with high purity, indistinguishable from those prepared via the conventional Ag-mediated route. All products were characterized by ^{1}H NMR, which confirmed the effectiveness of the ion exchange by showing equimolar amounts of methacrylate anions and organic cations (Figure S2–3). Furthermore, NMR analysis proved the effectiveness of the drying procedure, as the water content in all cases is comparable to the usual water content detected in hygroscopic deuterated solvents such as DMSO-d_6. All synthetized pILs were liquid at room temperature.

To guide the selection of ionic liquid cations for 3D-printable resins, two structurally distinct families were considered: imidazolium and tetraalkylammonium. Within the imidazolium series, $[C_2MIM]^+$, $[C_6MIM]^+$, and $[C_{10}MIM]^+$ share a polar imidazole core but differ in the length of the alkyl substituent, allowing systematic tuning of lipophilicity, steric bulk, and ionic mobility. Two tetraalkylammonium cations, $[N_{2222}]^+$ and $[N_{8888}]^+$, were included as fully aliphatic analogs with markedly different chain lengths and charge shielding, providing a complementary perspective on the effect of spherical, non-aromatic cations on resin properties. To rationalize their behavior in the polymer matrix, molecular volume and lipophilicity (cLogP) were computed for all cations (Table 2). In both series, longer alkyl chains increase molecular volume and lipophilicity, which can reduce ionic mobility due to stronger segregation of hydrophobic domains and longer ion-pair distances. Thus, ion transport is governed by a balance between reduced Coulombic interactions and enhanced microphase organization that can either promote or hinder conductivity depending on the specific cation structure. Interestingly, $[N_{2222}]^+$ exhibits slightly higher lipophilicity than $[C_{10}MIM]^+$, likely due to more effective charge shielding by its four ethyl chains compared to the single long chain of $[C_{10}MIM]^+$. Molecular volume trends also reflect structural differences: imidazolium cations increase nearly linearly with chain length while maintaining a compact polar core, whereas tetraalkylammonium ions are bulkier and more spatially diffuse, with $[N_{8888}]^+$ having the largest volume. These differences in steric size and shape are expected to influence both packing within the polymer network and ionic transport. Additional cations, including tetraphenylphosphonium, cetyltrimethylammonium, and hexadecylpyridinium, were initially screened but excluded due to poor solubility of their methacrylate salts in 3D-printable resins.

Table 2
Computed molecular volume and lipophilicity of the employed organic cations, together with the molecular weight of their methacrylate salt (MW_{pIL}).

Cation	Alkyl chain(s) length	Molecular volume (Å^3)	cLogP	MW_{pIL} (g/mol)
$[C_2MIM]^+$	2	107	- 3.328	196.25
$[C_6MIM]^+$	6	177	- 1.212	252.36
$[C_{10}MIM]^+$	10	245	+ 0.904	308.47
$[N_{2222}]^+$	2 (per chain)	162	+ 1.103	215.34
$[N_{8888}]^+$	8 (per chain)	580	+ 9.556	551.99

In order to explore the potential of the prepared pILs as photocurable ionic additives, they were mixed with a flexible and transparent PEG-based custom resin at different concentrations. PEG (in its monoacrylate and diacrylate versions) was selected to constitute 50 wt. % of the base resin, thanks to its well-recognized hydrophilicity and its ionic conduction properties [35,36]. All synthesized ionic liquids were fully miscible with the base resin. For each ionic liquid, several formulations were prepared at increasing molar concentrations (C), while keeping the concentration consistent across different cations. This strategy ensured that any observed differences in materials properties could be attributed to the chemical nature of the cation rather than to variations in ion concentration.

The mixtures were efficiently 3D printed using a common desktop VP 3D printer, after a preliminary optimization of the exposure times per layer. All 3D printed materials were optically transparent (Figure S4), and high printing resolution was achieved regardless of resins composition (Fig. 2). Despite the high ionic liquid fractions achievable in some formulations, all mixtures remained sufficiently fluid to ensure homogeneous recoating and defect-free printing. This behavior reflects the relatively low viscosity of the synthesized pILs and the presence of PEG-based monomers that act as effective reactive diluents. Qualitative observations during printing confirmed smooth layer formation and reliable curing under standard VP conditions.

A first limitation quickly emerged: the maximum amount of ionic liquid that can be incorporated is strongly constrained by its molecular weight. At high ionic liquid contents, the concentration of crosslinking species (HDDA and PEGDA) decreases substantially, which prevents proper 3D printing. For all ionic liquids except $[N_{8888}][MA]$, printability was lost only when the ionic liquid exceeded ~70–80 wt. %. In contrast, $[N_{8888}][MA]$ could not be printed even at 1 mmol/g (≈55 wt. %), a concentration at which all other ionic liquids were still printable. This anomaly is explained by the significantly larger molecular weight of $[N_{8888}]+$, which drastically reduces the total amount of photocurable groups per gram of formulation. With so few reactive species available, a stable crosslinked network cannot form. An additional explanation can be related to the steric hindrance of the bulky tetraoctylammonium cation, which limits network packing and polymerizable group accessibility, further preventing the formation of a stable crosslinked structure.

To rationalize these observations, we defined and reported in Table S3 for each formulation (see Supporting Information for mathematical definitions and demonstrations):

i) N_{TOT}^0, the total concentration of acrylate groups in the base resin (Equation S1),
ii) N_{TOT}, the total concentration of acrylate groups in any given resin (Equation S2),
iii) N_C^0, the total concentration of crosslinking acrylate groups in the base resin (Equation S3),
iv) N_C, the total concentration of crosslinking acrylate groups in any given resin (Equation S4),

By construction, both N_{TOT} and N_C depend linearly on the ionic liquid content C, with N_C always decreasing and N_{TOT} either increasing or decreasing depending on the balance between base resin composition and MW_{pIL}. Eliminating C leads to a direct linear relationship between N_C and N_{TOT} (Equation S5), describing a pencil of straight lines all intersecting at the coordinates of the blank resin (N_{TOT}^0 and N_C^0). The slope of each line depends uniquely on MW_{pIL} according to Eq. (2):

$$k_{pIL} = \frac{N_C^0}{N_{TOT}^0 - \frac{1000}{MW_{pIL}}} \quad (2)$$

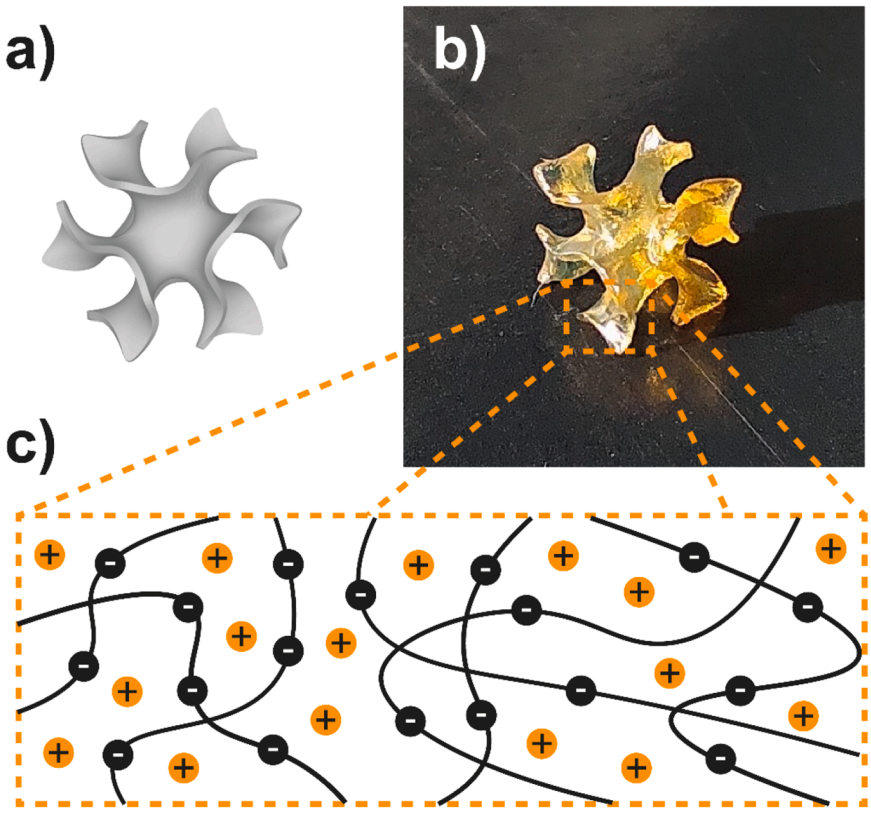

Fig. 2. Photopolymerization-based 3D printing of photocurable ionic liquid. Digital view of a gyroid cube (a) and the corresponding high-resolution 3D printed piece (b) obtained using the resin containing 3.0 mmol/g of $[N_{2222}][MA]$. The lateral size of the gyroid cube is 5 mm. The 3D printed material is composed of a crosslinked polyanionic network where positive ions ($[N_{8888}]^+$ in this case) can move when an external electric field is applied (c).

Plotting N_C vs. N_{TOT} (Fig. 3) shows that non-printable formulations cluster in a distinct region characterized by either very low N_C or very low N_{TOT}, thereby defining a printability window. Formulations with increasing ionic liquid content C fall along straight lines of slope k_{pIL} emerging from (N_{TOT}^0, N_C^0). Eq. (2) also predicts a critical case when $MW_{pIL} = \frac{1000}{N_{TOT}^0}$ (here 226 g/mol), for which the slope becomes undefined and the line turns vertical. Ionic liquids with lower MW_{pIL}, such as $[C_2MIM][MA]$ and $[N_{2222}][MA]$, generate lines of positive slope, so that

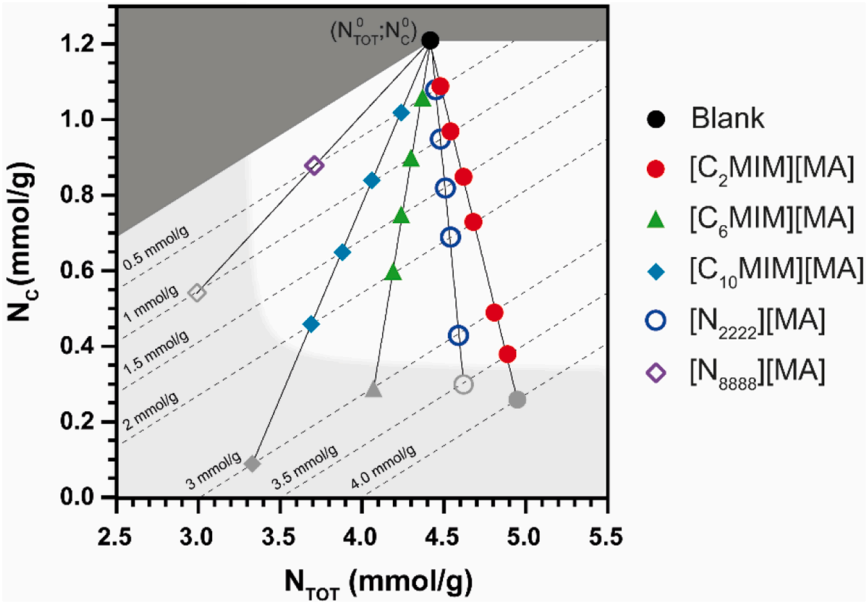

Fig. 3. Crosslinking acrylates (N_C, mmol/g) vs. total acrylate content (N_{TOT}, mmol/g) for the tested formulations. Grey points correspond to non-printable formulations, while the shaded area marks the experimentally identified non-printable region. Dark grey region represents formulations that cannot be achieved with the proposed base resin, delimited by the lines corresponding to MW_{pIL} of 0 and ∞. Each set of formulations lies on straight lines starting from the blank resin composition, with slope equal to k_{pIL}. Dashed lines connect points with the same molar concentration of ionic liquid.

N_{TOT} increases with increasing C, enabling higher printable concentrations. Moreover, formulations with the same molar concentration of ionic liquid lie on parallel lines, which intersect the x-axis precisely at that concentration.

This graphical representation, combined with the experimentally identified printability limits, allows one to predict in advance the maximum printable concentration of a given monofunctional additive in a given resin and to design the base resin composition accordingly, to extend the printable range. Bulky cations such as $[N_{8888}]^+$ illustrate the limitation of this design space: while they can be incorporated, their high MW and poor crosslinking compatibility preclude reliable printing and property mapping. This boundary condition further reinforces the relevance of N_C—N_{TOT} design maps.

The effectiveness of the photopolymerization taking place during VP was assessed by ATR-FTIR spectroscopy (Figure S5). In all cases, no significant (meth)acrylate C=C absorption (~ 1635 cm^{-1}) remains after printing and 1 h post-cure, indicating quantitative consumption of the vinyl groups and effective tethering of the ionic-liquid anions to the network. As it could be expected, as the pIL concentration increases, the peaks corresponding to the vibration frequencies of methacrylate anions gradually increase, while those related to the base resins components consistently decrease. In particular, a gradual reduction of the intensity of the peak related to the carbonyl stretching in carboxylate ions at 1550 cm^{-1} is accompanied by a gradual decrease in the intensity of the ester C=O stretching of acrylate esters at 1720 cm^{-1}. Parallelly, the C—O stretching frequency shifts to higher wavenumbers (1095 cm^{-1} to 1165 cm^{-1}). This behaviour is totally coherent with the electronic features of the carbonyl groups in both cases: in (meth)acrylate esters, the carbonyl group retains strong double-bond character, leading to a high C=O stretching frequency, while the C–O stretching appears at lower frequencies. In contrast, in methacrylate anions the negative charge is delocalized over both oxygen atoms, reducing the double-bond character of the carbonyl and lowering its stretching frequency, but increasing the bond strength and therefore the stretching frequency of the C–O bonds [37]. An additional difference can be detected by looking at the peaks related to aliphatic CH_2 groups (between 2800 and 3000 cm^{-1}), mostly related to PEG chains in the base resin, whose intensity increases when the added pIL contains long aliphatic chains (such as for $[C_{10}MIM]^+$ and $[N_{8888}]^+$), decreases when the added pIL has a short aliphatic chain ($[C_2MIM]^+$), and remains stable for $[C_6MIM]^+$ and $[N_{2222}]^+$, whose CH_2 content is comparable to the ones of PEG, HEMA and HDDA. Finally, a large peak above 3000 cm^{-1} related to H-bonded hydroxyl groups is observed to increase relatively to the other peaks when pIL concentration increases. While in the base resin this can be related to the free OH group of HEMA molecules, when the base resin is replaced by ionic liquids this peak is indeed related to absorbed water from the environment caused by the hygroscopic ionic liquids and their handling in uncontrolled atmosphere. This phenomenon does not appear to be detrimental; on the contrary, it may play a beneficial role. The absorbed water rapidly reaches a reproducible equilibrium level immediately after printing and remains stable over time (Figure S6). This equilibrium content correlates with both the ionic liquid fraction and the cation lipophilicity—more hydrophilic cations such as $[C_2MIM]^+$ exhibit slightly higher water uptake, whereas highly hydrophobic cations like $[N_{8888}]^+$ retain negligible amounts. Because this moisture level is stable and composition-dependent, its contribution to ionic conductivity is constant and implicitly included in the measured values. Therefore, the observed conductivity trends mainly reflect intrinsic differences in ion mobility rather than variations in hydration state.

The effectiveness and completeness of photopolymerization during the printing and post-curing processes were further assessed by evaluating the gel content of the formulations (Figure S7), which revealed consistent curing degrees of around 80 % across all 3D-printed materials, in line with recently reported methacrylate-based photocurable mixtures [38,39].

Then, tensile testing was performed to extract information regarding the mechanical behaviour of the 3D printed materials, and its connection with the molecular structure of the synthetized ionomers (Fig. 4, Figure S8 and Table S4). The incorporation of photocurable ionic liquids (pILs) into the acrylate-based resin leads to a dual effect on the mechanical properties of the printed networks. At low concentrations, the introduction of ionic groups promotes the establishment of ionic interactions between polymer chains, restricting chain mobility under mechanical stress and resulting in a clear enhancement of stiffness and strength compared to the blank resin. As the pIL concentration increases, however, the progressive dilution of the acrylate network and the steric/electrostatic perturbation induced by the bulky ionic moieties dominate, leading to a nearly linear decrease in stiffness and tensile strength. The elongation at break displays a less straightforward trend, remaining relatively stable or slightly enhanced at intermediate concentrations, consistent with the balance between additional ionic interactions and reduced network cohesion. Comparison of different cations shows that short and polar imidazolium-based pILs ($[C_2MIM][MA]$) are more effective in retaining mechanical performance, whereas longer alkyl chains or bulky ammonium cations ($[C_6MIM]^+$, $[C_{10}MIM]^+$, $[N_{2222}]^+$, $[N_{8888}]^+$) tend to accelerate the softening. Although the overall gel content remained around 80 % for all compositions, the effective network architecture was significantly affected by the IL content: increasing the concentration of monofunctional pILs reduces the relative abundance of crosslinking species and introduces steric/electrostatic disruptions, thereby lowering the effective crosslink density and resulting in mechanical softening even at similar curing degrees.

While conventional photopolymerized resins typically exhibit elastic moduli in the hundreds of MPa to GPa range, ionic polymers and ionic composites reported in the literature often suffer from poor mechanical robustness, with moduli in the kPa range that limit structural integrity and device integration. In contrast, our formulations reproducibly deliver MPa-level stiffness while retaining stretchability and flexibility, positioning them in an intermediate regime that is largely unexplored. This combination provides a rare balance: soft enough to allow deformation and ion transport, yet sufficiently robust to withstand handling, printing stresses, and practical use. Such a mechanical window is especially appealing for soft ionotronic devices, wearable sensors, and antistatic coatings, where both resilience and compliance are required.

To complement the mechanical characterization, ionic conductivity measurements were carried out on the printed materials containing different ionic liquids at different concentrations (Fig. 5 and Table S4). The comparative analysis of the resulting conductivity curves shows that, although the incorporation of ionic liquids generally leads to a significant increase in conductivity compared to the pristine material, the behavior of different cations varies markedly as a function of their structural and physicochemical properties. In particular, $[C_2MIM]^+$ exhibits an anomalous trend: after an initial increase in conductivity at low concentrations, the ionic conductivity stabilized in the 10^{-7}–10^{-8} S/cm range, regardless of its concentration.

This behavior can be rationalized by considering the properties reported in Table 2: $[C_2MIM]^+$ has the smallest molecular volume (107 $Å^3$) and a strongly hydrophilic character (cLogP = –3.328), which promotes intense interactions with the carboxylate groups covalently bound to the polymer backbone. Such interactions result in a strong ion pairing between the mobile cation and the fixed anionic sites of the crosslinked network, thereby limiting cation mobility and ultimately suppressing conductivity. At high loadings of $[C_2MIM]^+$, conductivity measurements show increased scatter, which can be attributed to the onset of heterogeneous ion pairing and possible microphase segregation between the ionic domains and the PEG-based network. This interpretation is indirect, as morphological characterization was beyond the scope of the present study, whose primary aim was to establish and validate the family of photocurable ionic liquids themselves. Moreover, such phase behavior is likely formulation-dependent and could vary with the chemistry and polarity of the photocurable resin, meaning that the

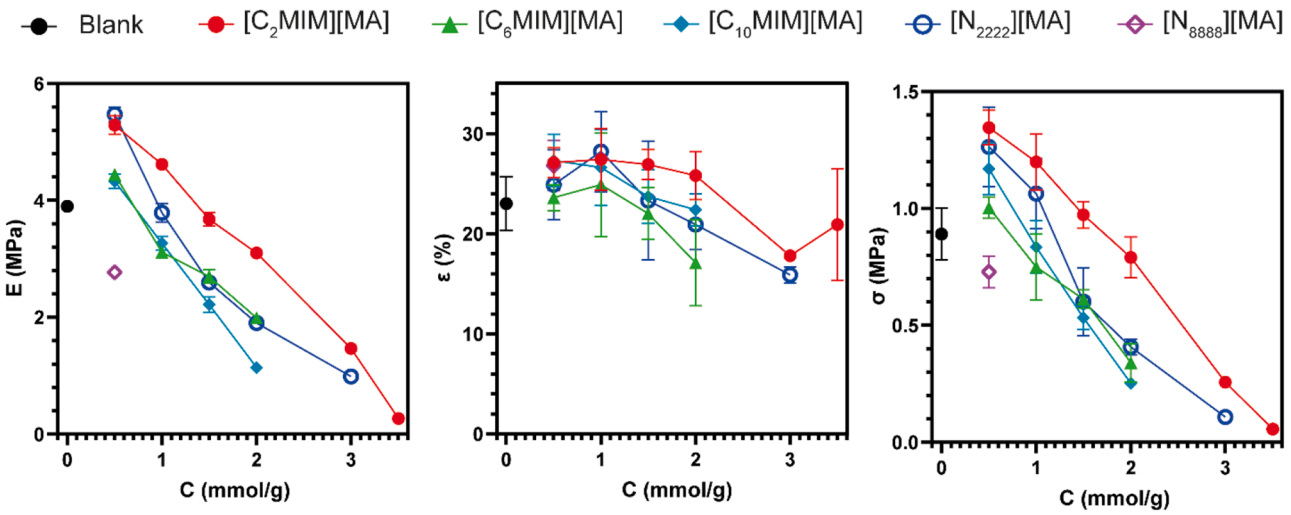

Fig. 4. Tensile properties of 3D printed materials as a function of the pIL concentration C. E = Young's modulus, ε = elongation at break and σ = tensile strength.

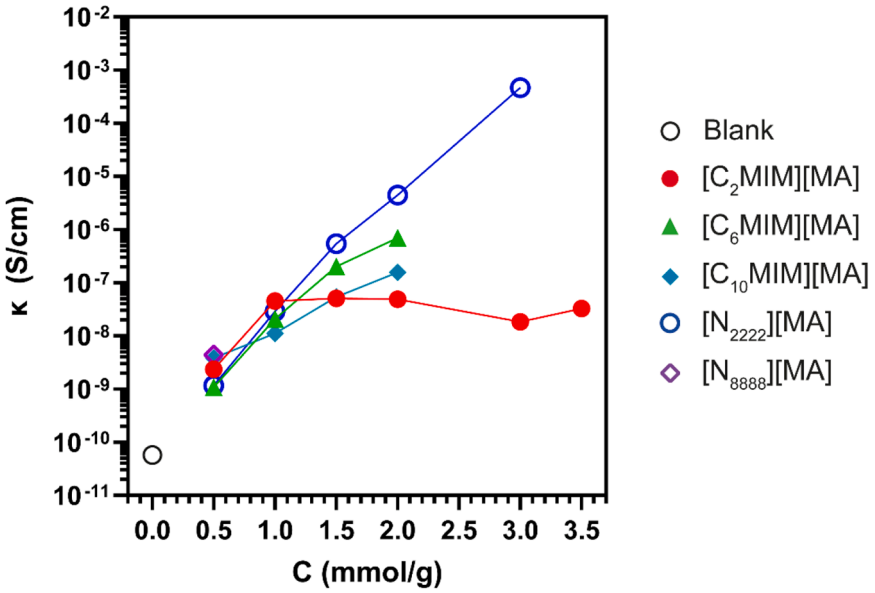

Fig. 5. Ionic conductivity of the 3D printed ionomers as a function of their molar concentration in the liquid resin, C.

observed heterogeneities may not be intrinsic to the ionic liquid structure. In contrast, cations with longer alkyl chains and higher lipophilicity, such as $[C_6MIM]^+$ and $[C_{10}MIM]^+$, are less prone to this trapping effect and display a more regular increase in conductivity with concentration. An even more pronounced enhancement is observed for $[N_{2222}]^+$, which combines an intermediate molecular volume (162 Å^3) with moderate lipophilicity (cLogP = +1.103), resulting in an optimal balance between mobility and compatibility with the polymer matrix.

When the measured electrical and mechanical properties are represented in the N_C–N_{TOT} space (Fig. 6), it is possible to correlate the materials properties with the features of the polymeric network. In fact, a consistent trend is observed for the mechanical properties, which are predominantly governed by the position in the N_C–N_{TOT} diagram, reflecting the architecture of the polymer network. In contrast, ionic conductivity is decoupled from the (N_C, N_{TOT}) coordinates and is instead governed by the cation structure. More hydrophobic and appropriately shielded cations tend to deliver higher conductivity, consistent with reduced ion pairing and enhanced charge-carrier mobility in the ion-rich microenvironment. Any residual dependence of the conductivity on crosslink density, when present, is comparatively weak and likely arises from changes in free volume and tortuosity that modulate ion mobility but do not overturn the cation-controlled ranking.

The N_C–N_{TOT} maps reveal not only the boundaries of printability but also the fundamental trade-offs between stiffness and ionic transport. Approaching the lower gray limit corresponds to reduced crosslink density and, consequently, lower modulus and strength, while moving upward and right increases mechanical robustness at the expense of marginally reduced conductivity. Importantly, these competing effects converge to define an operating window where VP formulations remain printable, mechanically resilient, and sufficiently conductive. Within this window, MPa-level stiffness coexists with room-temperature ionic conductivities in the 10^{-6}–10^{-4} S/cm range, without the need for conductive nanofillers or free IL additives, while retaining optical clarity and flexibility. This combination is rarely achieved in ion-conducting polymers, where conductivity is typically enhanced by blending free ILs or conductive fillers at the cost of transparency, softness, or printability. Here, ionic transport is instead engineered within the neat printable matrix by combining cation selection with network design in a physically meaningful parameter space. The result is a materials platform distinguished by chemical simplicity, modularity, and predictive

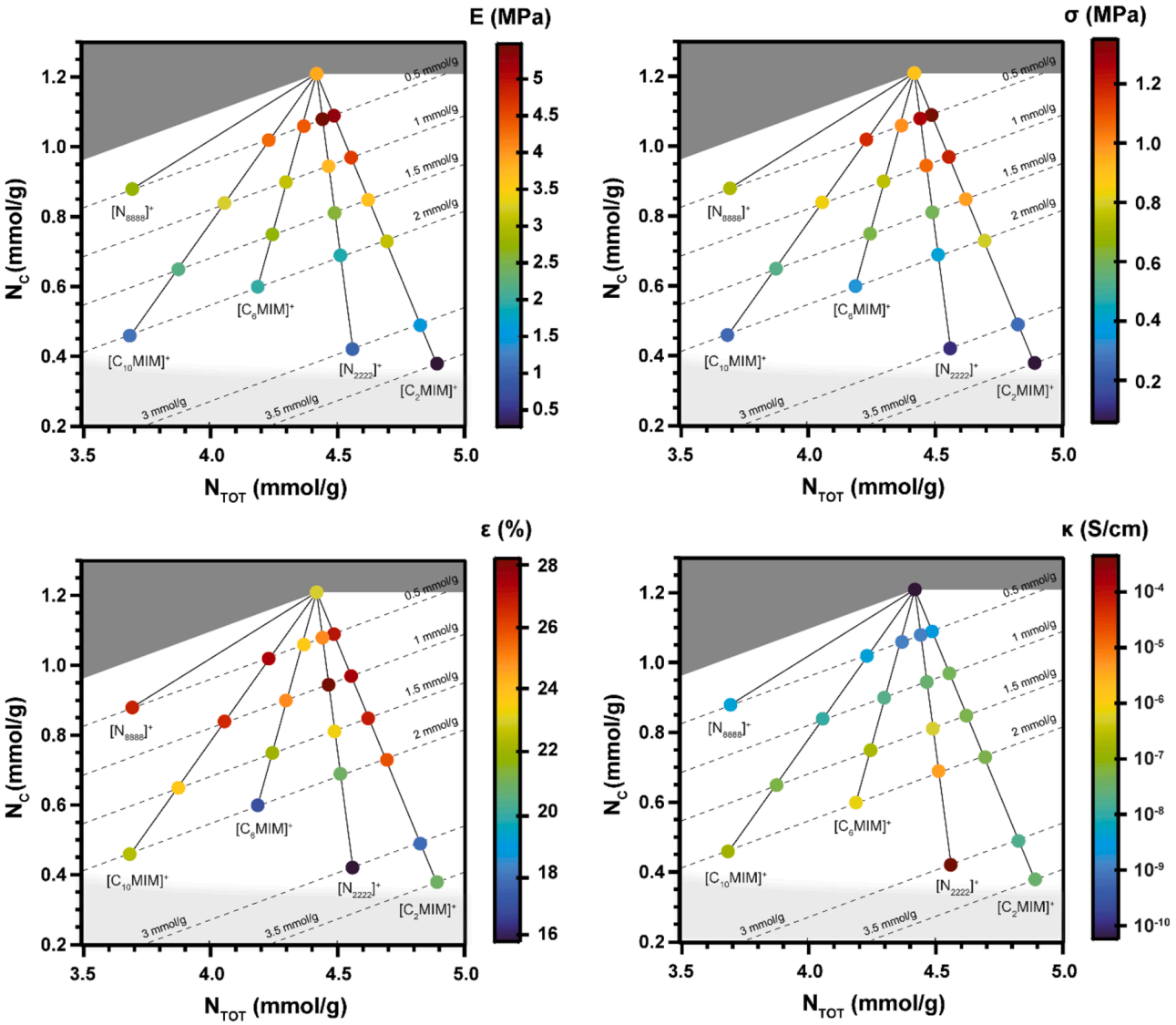

Fig. 6. Crosslinking acrylates (N_C, mmol/g) vs. total acrylate content (N_{TOT}, mmol/g) for the 3D-printable formulations, where data points are represented according to color scales on the basis of the measured Young's modulus (E), tensile strength (σ), elongation at break (ε) and bulk electrical conductivity (κ). As in Fig. 2, the shaded area marks the experimentally identified non-printable region and dark grey region represents formulations that cannot be achieved with the proposed base resin. Each set of formulations lies on straight lines starting from the blank resin composition, with slope equal to k_{pIL}. Dashed lines connect points with the same molar concentration of ionic liquid C.

control.

The formulation map also provides actionable levers for extending the printable–conductive window. Increasing N_C^0 through ionic crosslinkers or macro-crosslinkers preserves network connectivity at very high ionic liquid loadings; increasing N_{TOT}^0 via lower-MW reactive diluents or pILs raises the density of reactive groups per gram; tailoring cation hydrophobicity and steric environment reduces ion pairing while maintaining mechanical robustness. Each of these strategies shifts the base-resin point and steers formulation trajectories away from non-printable regions, enabling progressively higher IL incorporation without loss of transparency or processability.

Placed against application targets, the present window already encompasses antistatic and ESD-protection coatings and overlaps with soft-ionogel sensing regimes. At the same time, the design map charts clear pathways toward electrolyte-grade conductivities by combining ionic crosslinkers, cation designs that suppress ion pairing, and benign plasticization. Crucially, these advances can be pursued while remaining filler-free, transparent, and fully compatible with vat photopolymerization. Beyond the present systems, this framework establishes a general strategy for transforming ionic liquid additives from empirical modifiers into predictive design tools for multifunctional soft materials.

4. Conclusions

This study establishes a new strategy for the design of 3D-printable ion-conducting materials by introducing photocurable ionic liquids (pILs) in which the anion itself is polymerizable. This simple and modular chemical design allows ionic species to become covalently integrated into the polymer network during vat photopolymerization, thereby preventing liquid leakage and ensuring long-term structural stability. The synthesis of methacrylate-based pILs through ion-exchange reactions is straightforward, scalable, and adaptable to a wide variety of organic cations, highlighting the versatility and accessibility of the approach compared to conventional ionic liquid-based formulations that require complex synthetic steps or non-sustainable anions. By framing resin compositions in terms of two descriptors, the total acrylate content and the fraction contributed by crosslinkers, this work defines a quantitative printability window that rationalizes why

some formulations succeed while others fail. This framework not only captures the experimental behavior of diverse cations but also provides predictive levers for designing future formulations, including the possibility of incorporating ionic crosslinkers or reactive diluents to expand the printable range. Mechanical behavior was found to correlate strongly with crosslink density, with imidazolium-based pILs showing predictable linear scaling, while tetraalkylammonium systems deviated due to their intrinsic plasticizing effect. Ionic conductivity, in contrast, was determined predominantly by cation structure, with hydrophobicity and steric shielding minimizing ion pairing and enhancing charge mobility. This decoupling of mechanical integrity and ion transport demonstrates that both properties can be independently optimized by careful cation selection and network design. As a result, the printed ionic networks reported here occupy a unique regime in the soft materials landscape: they achieve MPa-level stiffness, elongations typical of soft networks, and room-temperature ionic conductivities in the 10^{-6}–10^{-4} S/cm range, while simultaneously retaining transparency, softness, and full processability by vat photopolymerization. Such a combination of properties is rarely achieved in ion-conducting polymers, which typically rely on free IL blending or conductive fillers that compromise optical clarity and printability. The combination of chemical simplicity, scalability, and predictive formulation design underscores the broader relevance of this approach as a platform for engineering functional printable ionic polymers. Its uniqueness lies in bridging the gap between classical ionic polymers and rigid photopolymers, providing a generalizable framework to design materials that are at once conductive, transparent, and mechanically robust. Future developments may extend this framework to higher-conductivity electrolytes through tailored cation designs and ionic crosslinkers, ultimately enabling filler-free, transparent, and processable materials for advanced applications in energy storage, wearable electronics, and low-voltage energy harvesting.

Associated content

Supporting Information. Supporting Information file includes NMR, FTIR and UV–VIS spectra, mathematical demonstrations, water weight content and degree of curing data and plots, and tensile stress-strain curves.

CRediT authorship contribution statement

Rosario Carmenini: Writing – original draft, Methodology, Investigation. **Alberto Sanz de Leon:** Writing – original draft, Investigation, Data curation. **Mauro Comes Franchini:** Writing – review & editing, Supervision. **Sergio Ignacio Molina:** Writing – review & editing, Supervision, Funding acquisition. **Mirko Maturi:** Writing – original draft, Methodology, Data curation, Conceptualization.

Declaration of competing interest

The authors declare that they have no known competing financial interests or personal relationships that could have appeared to influence the work reported in this paper.

Acknowledgements

MM acknowledges the University of Cádiz for his postdoctoral fellowship (2025–042/PU/POSTDOC-R3/CD). Aroma System S.R.L. is gratefully acknowledged for the financial support provided in the frame of RC's PhD studies (ref. DM 352/2022 – M4 C2 – Inv. 3.3 Next-GenerationEU). Funding from the University of Cádiz is also acknowledged (research group INNANOMAT, ref. TEP-946).

Supplementary materials

Supplementary material associated with this article can be found, in the online version, at doi:10.1016/j.apmt.2025.103018.

Data availability

Data will be made available on request.

References

[1] K. Kanishka, B. Acherjee, Revolutionizing manufacturing: a comprehensive overview of additive manufacturing processes, materials, developments, and challenges, J. Manuf. Process. 107 (2023) 574–619, https://doi.org/10.1016/J.JMAPRO.2023.10.024.
[2] M.A. Islam, M.H. Mobarak, M.I.H. Rimon, M.Z. Al Mahmud, J. Ghosh, M.M. S. Ahmed, N. Hossain, Additive manufacturing in polymer research: advances, synthesis, and applications, Polym. Test. 132 (2024) 108364, https://doi.org/10.1016/J.POLYMERTESTING.2024.108364.
[3] L. Zhou, J. Miller, J. Vezza, M. Mayster, M. Raffay, Q. Justice, Z. Al Tamimi, G. Hansotte, L.D. Sunkara, J. Bernat, Additive manufacturing: a comprehensive review, Sensors 24 (2024) 2668, https://doi.org/10.3390/S24092668.
[4] Y. Li, W. Wang, F. Wu, R.K. Kankala, Vat polymerization-based 3D printing of nanocomposites: a mini review, Front. Mater. 9 (2023) 1118943, https://doi.org/10.3389/FMATS.2022.1118943/BIBTEX.
[5] A. Bagheri, J. Jin, Photopolymerization in 3D printing, ACS. Appl. Polym. Mater. 1 (2019) 593–611, https://doi.org/10.1021/ACSAPM.8B00165/ASSET/IMAGES/LARGE/AP-2018-00165Y_0007.JPEG.
[6] M. Pagac, J. Hajnys, Q.P. Ma, L. Jancar, J. Jansa, P. Stefek, J. Mesicek, A review of Vat photopolymerization Technology: materials, applications, challenges, and future trends of 3D printing, Polymers. (Basel) 13 (2021) 598, https://doi.org/10.3390/POLYM13040598.
[7] M. Maturi, S. Maturi, A. Sanz de León, L. Migliorini, M. de la Mata, T. Benelli, L. Giorgini, P. Milani, M. Comes Franchini, S.I. Molina, Enhanced properties of 3D-printed graphene oxide nanocomposites through itaconic acid polyester grafting, ACS. Appl. Polym. Mater. 7 (2025) 4371–4382, https://doi.org/10.1021/ACSAPM.5C00014/ASSET/IMAGES/LARGE/AP5C00014_0006.JPEG.
[8] M. Maturi, L. Migliorini, S.M. Villa, T. Santaniello, N. Fernandez-Delgado, S. I. Molina, P. Milani, A. Sanz de León, M.C. Franchini, 3D-Printing of highly piezoelectric barium titanate polymer nanocomposites with surface-modified nanoparticles at low loadings, Adv. Funct. Mater. 35 (2025) 2407077, https://doi.org/10.1002/ADFM.202407077.
[9] X. Fan, S. Liu, Z. Jia, J.J. Koh, J.C.C. Yeo, C.G. Wang, N.E. Surat'man, X.J. Loh, J. Le Bideau, C. He, Z. Li, T.P. Loh, Ionogels: recent advances in design, material properties and emerging biomedical applications, Chem. Soc. Rev. 52 (2023) 2497–2527, https://doi.org/10.1039/D2CS00652A.
[10] C.C. Yan, W. Li, Z. Liu, S. Zheng, Y. Hu, Y. Zhou, J. Guo, X. Ou, Q. Li, J. Yu, L. Li, M. Yang, Q. Liu, F. Yan, Ionogels: preparation, properties and applications, Adv. Funct. Mater. 34 (2024) 2314408, https://doi.org/10.1002/ADFM.202314408.
[11] S.M. Villa, V.M. Mazzola, T. Santaniello, E. Locatelli, M. Maturi, L. Migliorini, I. Monaco, C. Lenardi, M. Comes Franchini, P. Milani, Soft piezoionic/piezoelectric nanocomposites based on ionogel/BaTiO3 nanoparticles for low frequency and directional discriminative pressure sensing, ACS Macro Lett. 8 (2019) 414–420, https://doi.org/10.1021/ACSMACROLETT.8B01011/SUPPL_FILE/MZ8B01011_SI_001.PDF.
[12] S. Pan, M. Yao, J. Zhang, B. Li, C. Xing, X. Song, P. Su, H. Zhang, Recognition of ionic liquids as high-voltage electrolytes for supercapacitors, Front. Chem. 8 (2020) 261, https://doi.org/10.3389/fchem.2020.00261.
[13] G. Zhao, B. Lv, H. Wang, B. Yang, Z. Li, R. Junfang, G. Gui, W. Liu, S. Yang, L. Li, Ionogel-based flexible stress and strain sensors, Int. J. Smart. Nano Mater. 12 (2021) 307–336, https://doi.org/10.1080/19475411.2021.1958085.
[14] Y. Xu, L. Chen, J. Chen, X. Chang, Y. Zhu, Flexible and transparent pressure/temperature sensors based on ionogels with bioinspired interlocked microstructures, ACS. Appl. Mater. Interfaces. 14 (2022) 2122–2131, https://doi.org/10.1021/ACSAMI.1C22428/SUPPL_FILE/AM1C22428_SI_001.PDF.
[15] M. Wang, J. Hu, M.D. Dickey, Tough ionogels: synthesis, toughening mechanisms, and mechanical properties-A perspective, JACS. Au 2 (2022) 2645–2657, https://doi.org/10.1021/JACSAU.2C00489/ASSET/IMAGES/LARGE/AU2C00489_0009.JPEG.
[16] M. Gillono, A. Chiappone, L. Mendola, M.Gomez Gomez, L. Scaltrito, C.F. Pirri, I. Roppolo, Study on the printability through digital light processing technique of ionic liquids for CO_2 capture, Polymers. (Basel) 11 (2019) 1932, https://doi.org/10.3390/polym11121932.
[17] S. Nechausov, A. Ivanchenko, O. Morozov, A. Miriyev, I. Must, O. Platnieks, M. Jurinovs, S. Gaidukovs, A. Aabloo, M. Kovač, B. Bulgakov, Effects of ionic liquids and dual curing on vat photopolymerization process and properties of 3d-printed ionogels, Addit. Manuf. 56 (2022) 102895, https://doi.org/10.1016/J.ADDMA.2022.102895.
[18] S. Miralles-Comins, M. Zanatta, V. Sans, Advanced formulations based on poly (ionic liquid) materials for additive manufacturing, (2022). https://doi.org/10.3390/polym14235121.

[19] K.R. Hossain, P. Jiang, X. Yao, X. Yang, D. Hu, X. Wang, Ionic liquids for 3D printing: fabrication, properties, applications, J. Ion. Liq. 3 (2023) 100066, https://doi.org/10.1016/J.JIL.2023.100066.
[20] J. Wen, L. Zhou, T. Ye, Polymer ionogels and their application in flexible ionic devices, SmartMat 5 (2024) e1253, https://doi.org/10.1002/SMM2.1253.
[21] A.A. Shamsuri, S. Nurul, A.M. Jamil, K. Abdan, M. Vannini, L. Sisti, A brief review on the influence of ionic liquids on the mechanical, thermal, and chemical properties of biodegradable polymer composites, Polymers. (Basel) 13 (2021) 2597, https://doi.org/10.3390/POLYM13162597.
[22] M.P. Scott, M. Rahman, C.S. Brazel, Application of ionic liquids as low-volatility plasticizers for PMMA, Eur. Polym. J. 39 (2003) 1947–1953, https://doi.org/10.1016/S0014-3057(03)00129-0.
[23] Y. Yahata, K. Kimura, Y. Nakanishi, S. Marukane, T. Sato, Y. Tsujii, K. Ohno, Control of phase separation in polystyrene/ionic liquid-blended films by polymer brush-grafted particles, Langmuir 35 (2019) 3733–3747, https://doi.org/10.1021/ACS.LANGMUIR.8B03891/SUPPL_FILE/LA8B03891_SI_001.PDF.
[24] A. Kotsiras, J. Whitley, E. Orozco, C.A. Guymon, Influence of ionic liquid and light intensity on a polymer nanostructure formed in lyotropic liquid crystalline templates, ACS. Appl. Polym. Mater. 6 (2024) 2442–2452, https://doi.org/10.1021/ACSAPM.3C01812/ASSET/IMAGES/LARGE/AP3C01812_0010.JPEG.
[25] K. Lee, Y. Shang, V.A. Bobrin, R. Kuchel, D. Kundu, N. Corrigan, C. Boyer, K. Lee, V. A. Bobrin, N. Corrigan, C. Boyer, Y. Shang, D. Kundu, R. Kuchel, 3D Printing nanostructured solid polymer electrolytes with high modulus and conductivity, Adv. Mater. 34 (2022) 2204816, https://doi.org/10.1002/ADMA.202204816.
[26] J. Jeddi, J. Niskanen, B.H. Lessard, J. Sangoro, Ion transport in polymerized ionic liquids: a comparison of polycation and polyanion systems, Faraday Discuss. 253 (2024) 426–440, https://doi.org/10.1039/D4FD00070F.
[27] A. Mauri, P. Kiefer, P. Neidinger, T. Messer, N.M. Bojanowski, L. Yang, S. Walden, A.N. Unterreiner, C. Barner-Kowollik, M. Wegener, W. Wenzel, M. Kozlowska, Two- and three-photon processes during photopolymerization in 3D laser printing, Chem. Sci. 15 (2024) 12695, https://doi.org/10.1039/D4SC03527E.
[28] D. Burgess, N. Li, N. Rosik, P.J. Fryer, I. McRobbie, H. Zhang, Z.J. Zhang, Surface-grafted poly(ionic liquid) that lubricates in both non-polar and polar solvents, ACS Macro Lett. 10 (2021) 907–913, https://doi.org/10.1021/ACSMACROLETT.1C00174/ASSET/IMAGES/LARGE/MZ1C00174_0006.JPEG.
[29] Y. Yahata, K. Kimura, Y. Nakanishi, S. Marukane, T. Sato, Y. Tsujii, K. Ohno, Control of phase separation in polystyrene/ionic liquid-blended films by polymer brush-grafted particles, Langmuir 35 (2019) 3733–3747, https://doi.org/10.1021/ACS.LANGMUIR.8B03891/SUPPL_FILE/LA8B03891_SI_001.PDF.
[30] J. Lu, F. Yan, J. Texter, Advanced applications of ionic liquids in polymer science, Prog. Polym. Sci. 34 (2009) 431–448, https://doi.org/10.1016/J.PROGPOLYMSCI.2008.12.001.
[31] F. Xu, Y. Su, B. Lin, Progress of Alkaline Anion exchange membranes for fuel cells: the effects of micro-phase separation, Front. Mater. 7 (2020) 514535, https://doi.org/10.3389/FMATS.2020.00004/BIBTEX.
[32] N. Ramaswamy, S. Mukerjee, Alkaline anion-exchange membrane fuel cells: challenges in electrocatalysis and interfacial charge transfer, Chem. Rev. 119 (2019) 11945–11979, https://doi.org/10.1021/ACS.CHEMREV.9B00157/ASSET/IMAGES/LARGE/CR9B00157_0011.JPEG.
[33] G. Ayalneh Tiruye, D. Muñoz-Torrero, J. Palma, M. Anderson, R. Marcilla, All-solid state supercapacitors operating at 3.5 V by using ionic liquid based polymer electrolytes, J. Power. Sources. 279 (2015) 472–480, https://doi.org/10.1016/J.JPOWSOUR.2015.01.039.
[34] J.P.C. Trigueiro, R.L. Lavall, G.G. Silva, Supercapacitors based on modified graphene electrodes with poly(ionic liquid), J. Power. Sources. 256 (2014) 264–273, https://doi.org/10.1016/J.JPOWSOUR.2014.01.083.
[35] S.N. 'Afini M. Johari, N.A. Tajuddin, H. Hanibah, S.K. Deraman, A review: ionic conductivity of solid polymer electrolyte based polyethylene oxide, Int. J. Electrochem. Sci. 16 (2021) 211049, https://doi.org/10.20964/2021.10.53.
[36] M.J. Reddy, J.S. Kumar, U.V. Subba Rao, P.P. Chu, Structural and ionic conductivity of PEO blend PEG solid polymer electrolyte, Solid. State Ion. 177 (2006) 253–256, https://doi.org/10.1016/J.SSI.2005.11.014.
[37] Y. Lu, J.D. Miller, Carboxyl stretching vibrations of spontaneously adsorbed and LB-transferred calcium carboxylates as determined by FTIR internal reflection spectroscopy, J. Colloid. Interface Sci. 256 (2002) 41–52, https://doi.org/10.1006/JCIS.2001.8112.
[38] L. Perea-Lowery, M. Gibreel, P.K. Vallittu, L. Lassila, Evaluation of the mechanical properties and degree of conversion of 3D printed splint material, J. Mech. Behav. Biomed. Mater. 115 (2021) 104254, https://doi.org/10.1016/J.JMBBM.2020.104254.
[39] S. Aktug Karademir, S. Atasoy, S. Akarsu, E. Karaaslan, Effects of post-curing conditions on degree of conversion, microhardness, and stainability of 3D printed permanent resins, BMC. Oral Health 25 (2025) 1–9, https://doi.org/10.1186/S12903-025-05664-5/TABLES/6.